analytical chemistry

pubs.acs.org/ac Article

Label-Free Monitoring of Coculture System Dynamics: Probing Probiotic and Cancer Cell Interactions via Infrared Spectroscopic Imaging

Yoon Jeong,[¶] Pei-Hsuan Hsieh,[¶] Yamuna Phal, Rohit Bhargava,* and Joseph Irudayaraj*

Cite This: https://doi.org/10.1021/acs.analchem.4c00894 Read Online

ACCESS | Metrics & More | Article Recommendations | Supporting Information

ABSTRACT: Evaluating the dynamic interaction of microorganisms and mammalian cells is challenging due to the lack of suitable platforms for examining interspecies interactions in biologically relevant coculture conditions. In this work, we demonstrate the interaction between probiotic bacteria (*Lactococcus lactis* and *Escherichia coli*) and A498 human cancer cells *in vitro*, utilizing a hydrogel-based platform in a label-free manner by infrared spectroscopy. The *L. lactis* strain recapitulated in the compartment system secretes polypeptide molecules such as nisin, which has been reported to trigger cell apoptosis. We propose a mid-infrared (IR) spectroscopic imaging approach to monitor the variation of biological components utilizing kidney cells (A498) as a model system cocultured with bacteria. We characterized the biochemical composition (i.e., nucleic acids, protein secondary structures, and lipid conformations) label-free using an unbiased measurement. Several IR spectral features, including unsaturated fatty acids, β-turns in protein, and nucleic acids, were utilized to predict cellular response. These features were then applied to establish a quantitative relationship through a multivariate regression model to predict cellular dynamics in the coculture system to assess the effect of nisin on A498 kidney cancer cells cocultured with bacteria. Overall, our study sheds light on the potential of using IR spectroscopic imaging as a label-free tool to monitor complex microbe-host cell interactions in biological systems. This integration will enable mechanistic studies of interspecies interactions with insights into their underlying physiological processes.

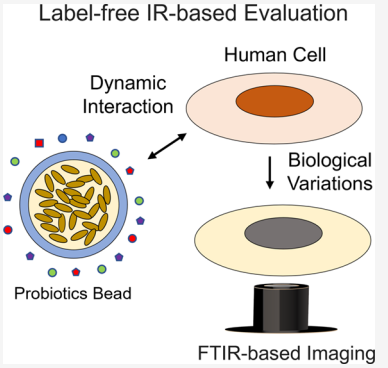

INTRODUCTION

The gut microbiome is one of the dominant microcosms in the human body which has the potential to modulate host metabolism and immune functions in physiological responses.[1,2] As specific bacterial groups have been detected in various tumor tissues, their ability to alter antitumor immunity and chemotherapeutic effects was found to affect cancer treatment.[3,4] Ample evidence supports the need for a deeper understanding of the implications of microbial alterations in cancer research.[5] However, a few studies at the *in vitro* level investigate the influence of specific microbial strains on mammalian cells in a dynamic format. For example, microfabrication systems have reported the potential of studying dynamic species compartments and interactions, providing insights into the intricate interplay between bacteria and mammalian cells.[6−8] However, several technical challenges arise from the spatial complexity of coculture systems and the integration of analytical techniques for measuring fluctuated chemical changes in interspecies (i.e., microbe and host cell) interactions. Given the lack of *in vitro* coculture systems, foremost, an analytical technique that can quantitatively explain the overall correlation between microbes and host cells will facilitate the monitoring of host−cell interactions *in situ*.

Infrared (IR) spectroscopic imaging with different sampling techniques combined with chemometrics has helped advance the understanding of biochemical information. With its high sensitivity, cellular spatial resolution,[9,10] improved detection limits,[11] and *in situ* assessment, IR spectroscopy has been used for monitoring different phases of cell cycle and cellular metabolism as well as an alternative digital pathological tool in the clinics.[10,12−17] Since IR absorbance presents a strong optical signal related to molecular composition, this technique provides qualitative and quantitative information on proteins, lipids, carbohydrates, and nucleic acids, and their secondary structures via spectral features such as peak locations, heights, and integrated areas.[18,19] Current studies using Fourier transform (FT)-IR spectroscopy to understand bacteria include bacterial strain identifications, metabolism, growth processes, stress, fermentation, and food quality and safety.[20−31] Despite the advances in the field, integrating *in*

Received: February 16, 2024
Revised: June 4, 2024
Accepted: June 17, 2024

Scheme 1. Overview of Study Model Depicting Dynamic Interactions between Probiotic Bacteria and Cancer Cells[a]

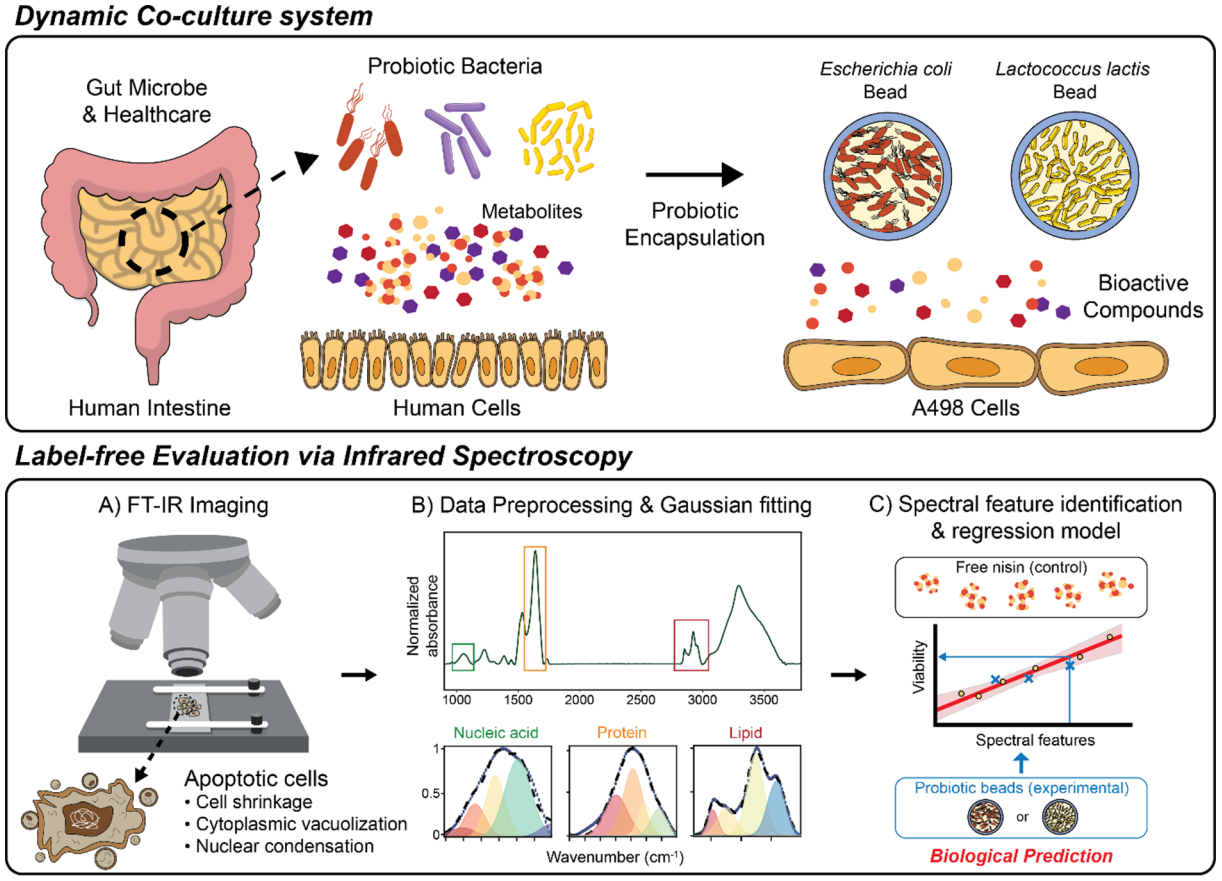

[a]A dynamic co-culture system is used to assess the indirect influence of probiotic bacteria toward mammalian cells (A498 cells) through bioactive molecules. IR spectroscopy with imaging was applied to record changes to macromolecules within A498 cells. Results are then analyzed by spectra deconvolution and chemometrics.

vitro coculturing system and label-free analytical approaches has not progressed yet to study the mechanism of bacteria and host cells in specific niches.

Here, we demonstrate an integrated approach to elucidate the dynamic interactions between probiotic bacteria and cancer cells at the *in vitro* level. The proof-of-concept schematic (Scheme 1) depicts the observation of reciprocal interaction between two interspecies and the integration of label-free FT-IR spectroscopy imaging to evaluate biological variations on cancer cells. A hydrogel-based compartment system was used for coculturing probiotic bacteria with cancer cells.[32−35] Two representative wild-type strains, *E. coli* and *L. lactis*, were selected and recapitulated in hydrogel-shell beads for colonization. Secondary metabolite molecules secreted from bacterial colonies in the encapsulant have the potential to trigger biological variations in A498 cancer cells by passing through the hydrogel barrier. Specifically, *L. lactis* strain produces nisin (i.e., peptidic toxin), which has been reported to cause cell apoptosis[36] Given the challenge in characterizing the physiological behavior of cells without the assistance of bioassays, label-free IR spectroscopic imaging was introduced to study the overall biological changes triggered by nisin. To identify critical spectral features related to nisin-inducing apoptosis, the correlation between conventional biochemical measurements and featured IR absorbance was established as a calibration curve using a multivariate regression model. Overall, we show that the combination of the relative quantity and conformation of macromolecules can reflect the degree of nisin-inducing cellular variations in a label-free manner using IR spectroscopy.

EXPERIMENTAL METHODS

Probiotics Hydrogel-Shell Encapsulation. Encapsulation techniques were followed by previously reported methods.[34] Briefly, bacteria cultured to the mid-exponential phase were mixed with 3 wt % of alginate solution. A needle-based extrusion method was used to fabricate alginate hydrogels gelled into a 0.1 M $CaCl_2$ solution. The gelled hydrogel beads containing bacteria were transferred to a low concentration of alginate solution (<0.1 wt %). Immediately, the concentration of the alginate solution was increased by up to 0.5 wt %. The reaction vessel containing hydrogel beads was shaken to prevent agglomeration and an excessive amount of deionized (DI) water was added. The hydrogel core−shell beads were rinsed three times with DI water. Detailed processes were noted in supporting materials (Figure S1 and Supplementary Note 1).

Co-Culturing Bacteria Bead with Mammalian Cells. Human renal carcinoma cell line A498 was purchased from ATCC and used for all *in vitro* coculture studies. The cells were grown in Eagle's MEM with L-glutamine (EMEM; ATCC) with 10% fetal bovine serum (FBS; Gibco), supplemented with 1% penicillin/streptomycin (Lonza). Cells were maintained in a CO_2 humidified incubator (37 °C, 5% CO_2). Coculture

https://doi.org/10.1021/acs.analchem.4c00894
Anal. Chem. XXXX, XXX, XXX−XXX

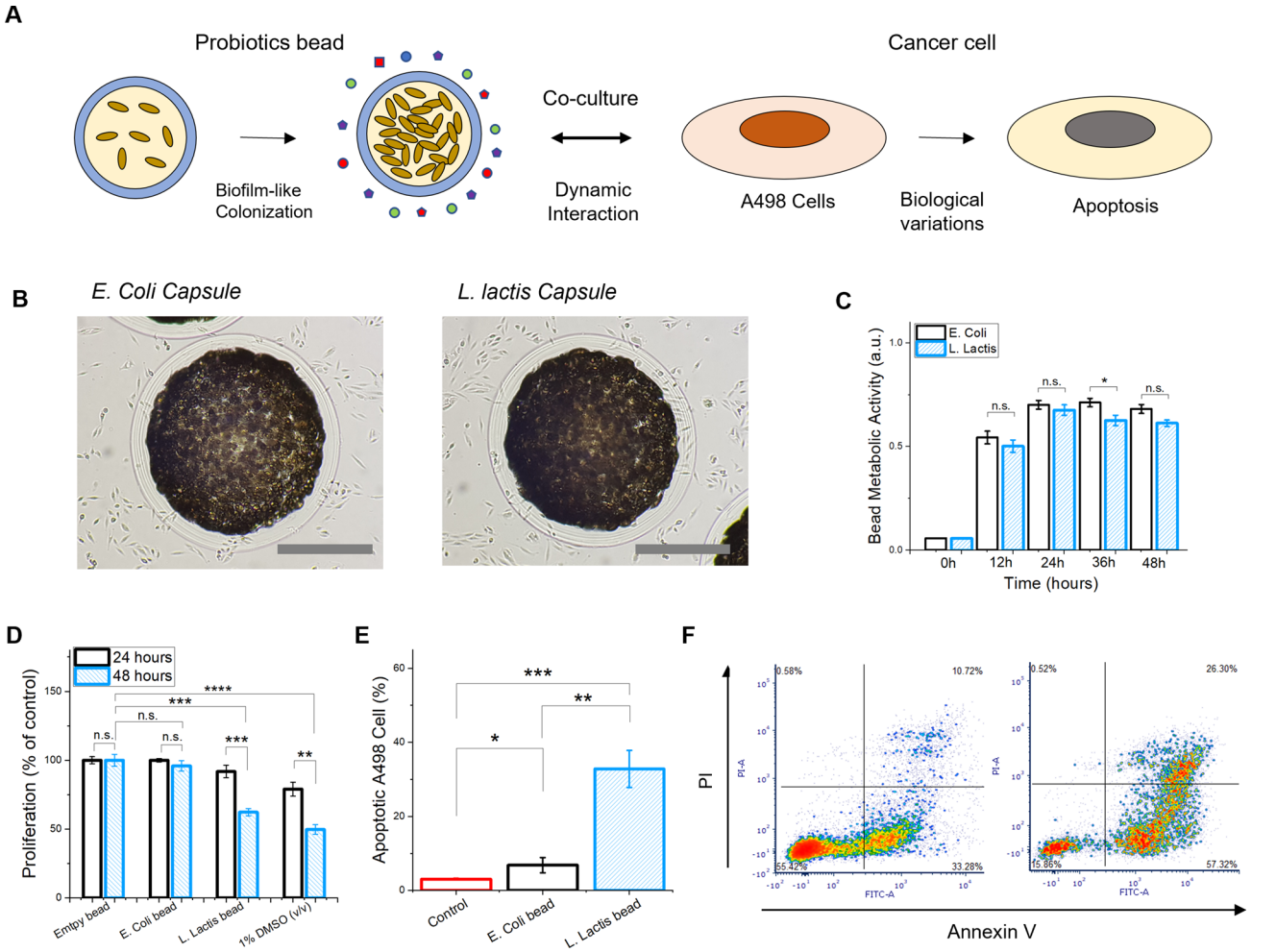

Figure 1. Co-culturing probiotic hydrogel bead and cancer cells. (A) Schematic of a dynamic coculture system. (B) Microscopic image of *E. coli* bead (left) and *L. lactis* (right) bead, cocultured with A498 cells after 24 h of incubation. Scale bar = 500 μm. (C) Metabolic activity comparison of bead encapsulated with *E. coli* or *L. lactis* as a function of time (additional explanation in Supplementary Note 1). (D) Proliferation of A498 cells cocultured with bead encapsulated with *E. coli* or *L. lactis* at 24 and 48 h. Empty bead and DMSO (1% v/v) served as negative and positive controls, respectively. (E) Percentage of apoptotic cells cocultured with probiotic bead at 24 h. (F) Flow cytometry plots of A498 cells, which were cocultured with *L. lactis* bead for 24 and 48 h to show cell apoptosis.

experiments with bacteria beads were conducted without antibiotics (penicillin/streptomycin). Bacteria hydrogel beads were fabricated with an average core-bead diameter of 500 and 100 μm of the shell thickness. The effect of probiotic (*E. coli* and *L. lactis*) bead and nisin (Sigma, N5764) on cell proliferation was measured by WST-1 assay (Roche Applied Science). Morphological features and nucleus condensation by DAPI (2-(4-amidinophenyl)-6-indolecarbamidine, Sigma) staining were observed using an inverted fluorescence microscope (Leica DMI3000B) after coculture.

Spectral Feature Selection and Multivariate Regression Model. To determine the characteristic spectral features that reflect on the overall cell responses, an estimate of the predictor importance was generated in MATLAB R2020a by the predictor importance function with AUC utilizing all the wavenumbers as input.[37]

This helps remove redundant wavenumbers that have an insignificant contribution between each experimental group. Once the spectral features were identified, the quantitative relationship between spectral features and cell viability was established. We adopt a multivariable regression model containing an intercept term (C), linear and squared terms for each predictor, and all products of pairs of distinct predictors. The analyses were performed using the film function.[38] The regression model is expressed by the equation given below.

$$E(Y|X_1, X_2, \ldots, X_p) = \mu(X) = C + \sum \beta_i X_i$$

where the predictor variables (X_p) are the area under the curve (AUC) for three nucleic acid-related peaks at 1055, 1080, and 1240 cm^{-1} and the ratio of AUC_{1080}/AUC_{1240}, four protein secondary structures, and lipid-related peaks at 2852 and 2923 cm^{-1} and their ratio (AUC_{2852}/AUC_{2923}). The correlated response variable is the recorded cell viability from the WST-1 assay for different control groups.

Statistical Analysis for Experimental Results. Experiments were performed in triplicate. The results were expressed as mean ± standard deviation (s.d.) and analyzed for correlation and differences using unpaired Student's *t*-test or one-way ANOVA with a post hoc test followed by posthoc comparisons using the Tukey's method (GraphPad prism 9.0.). *P* values with asterisks (<0.05) were considered statistically significant as follows *$p < 0.05$; **$p < 0.01$; ***$p < 0.001$; ****$p < 0.0001$.

https://doi.org/10.1021/acs.analchem.4c00894
Anal. Chem. XXXX, XXX, XXX−XXX

RESULTS AND DISCUSSION

Dynamic Co-Culturing of Probiotic Beads and Cancer Cells. The schematic illustration in Figure 1A depicts probiotic hydrogel beads cocultured with A498 cells. Various bioactive compounds secreted from the hydrogel encapsulant of microorganisms diffuse through a hydrogel barrier, while a high density of microbes remains stably colonized without leakage to the surrounding in the 3D polysaccharide matrix. This approach circumvents the major challenge of having completely entrapped bacteria in hydrogels by preventing leakage, which can lead to the overgrowth of uncontrolled bacterial populations in culture media (Figure S1 and Supplementary Note 1).[32,34] As shown in Figure 1B, A498 cells were cocultured with two probiotic beads. We selected *E. coli* as a comparison group for investigating the degree of bacteriocin-inducing cellular variations and compared the metabolic status of both *E. coli* and *L. lactis* beads in culture medium to verify the cultivability and sustenance (Figure 1C). The increase in metabolic activities was very similar in both microorganisms. However, morphological variations in A498 cells cocultured with *L. lactis* probiotic beads were not distinct compared to that of the *E. coli* hydrogel group after coculturing for 24 h (Figure S2).

To ascertain certain changes caused by probiotic beads, we conducted biological assays. We found that A498 cell proliferation from the WST-1 assay was significantly inhibited after 24 h of coculturing with the *L. lactis* beads (Figure 1D). On the other hand, any significant changes in A498 cells were not observed by coculturing with the *E. coli* beads even after 48 h of incubation. As initially designed for the study of bacteriocin-inducing cellular variations, the cytotoxic effect could be associated with *L. lactis* contributing to the production of a variety of active substances, one of which is nisin.[36,39,40] Additionally, we verified nisin can be produced and released from *L. lactis* colonies in the hydrogel structure through LC-MS analysis of the culture supernatant of *L. lactis* beads in medium (Figure S4). The result of coculturing *L. lactis* bead with A498 cells indicated the overall proportion of apoptotic cells significantly increased compared to the *E. coli* bead group (Figure 1E). The population of early and late apoptotic cells increased in coculture with *L. lactis* beads (Figures 1F and S5). Distinct changes such as cell shrinkage, cytoplasmic vacuolization, and nuclear condensation can also be exhibited from apoptotic cells. These cellular changes on A498 cells were more apparently observed after 60 h of coculture with *L. lactis* beads (Figure S5). As found in the experimental results, bioactive compounds including peptidic toxins produced from the *L. lactis* beads pose stress on the A498 cells. However, still, a question remains on the indirect impact caused by *L. lactis* colonies entrapped in the structure where nisin produced from *L. lactis* can be a major factor in triggering cellular apoptotic death. Further, we asked whether the cytotoxic effect on A498 cells could result from the secretion of secondary metabolites from *L. lactis* colonies since there are various bioactive compounds secreted from probiotics.

Infrared Spectral Evaluation of Biomolecular Changes Induced during Cell Apoptosis. There are several phenomena that are reported to be associated with cell apoptosis such as conformational changes of the nucleic acids, proteins, and lipids due to the morphological changes, nuclear fragmentation, chromatin condensation, and the disorganization of the lipids on the cell membrane and around the nucleus.[41−44] Typically, it requires a combination of assays with cellular sample preparation and specific biomarker staining to interpret the apoptotic features, such as distinct biochemical events during the programmed cell death.[45−47] However, cross-referencing different assays could lead to inconsistencies in the assessment of the apoptotic index. Since there are prominent changes in nucleic acids, protein secondary structures, and lipids during cell apoptosis, as an initial assessment, we compare the spectral regions that relate to these hallmarks with Gaussian curve fitting for specific molecules (Table S1). In Figure 2, the area under the curve

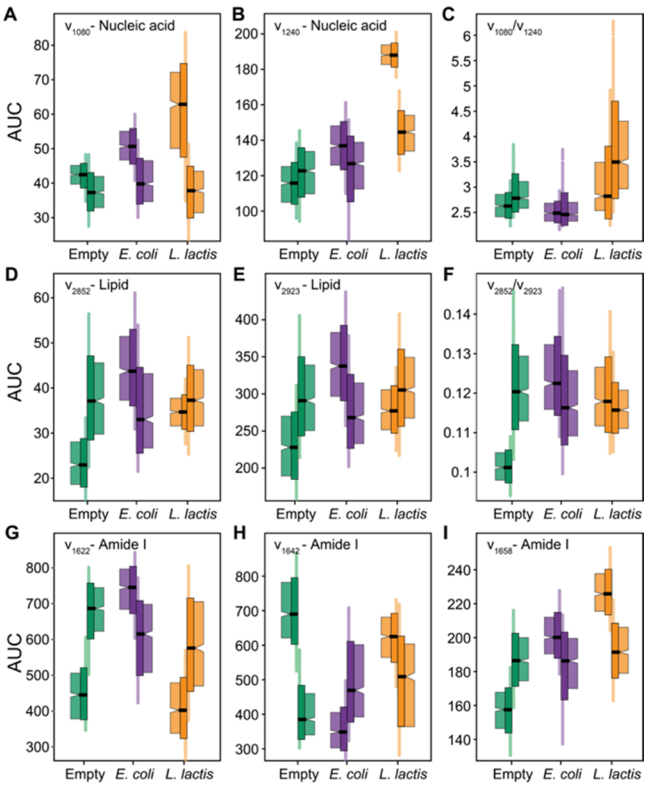

Figure 2. Comparison of AUC at specific spectral features with temporal changes at 24 h (left) and 48 h (right) in A498 cells treated with empty hydrogel beads, *E. coli* beads and *L. lactis* beads. The chosen wavenumbers correspond to (A−C) nucleic acids, (D−F) lipids, and (G−I) protein secondary structures. Box plots depict the interquartile range with marked median and whiskers extend to 1.5× the interquartile range beyond the first and third quartiles.

(AUC) related to nucleic acids, lipids, and protein secondary structures is shown as box plots. From Figure 2A, B, it can be seen that there is a distinct increase at the bands, 1080 and 1240 cm^{-1}, after incubating with *L. lactis* bead for 24 h, while the values decrease at 48 h (Figure S6). These two bands usually correspond to the symmetric and asymmetric vibrational modes of the phosphodiester groups on the nucleic acids or the hydrophilic heads in the phosphorylated lipids.[42] The increasing values may be related to a higher accumulation of single-stranded DNA or an increased formation of free phosphate groups released from the DNA or membrane phospholipid head groups during cell apoptosis. However, as apoptosis progresses, the breakdown of nucleic acids into small fragments occurs. This can result in the loss or condensation of

https://doi.org/10.1021/acs.analchem.4c00894
Anal. Chem. XXXX, XXX, XXX−XXX

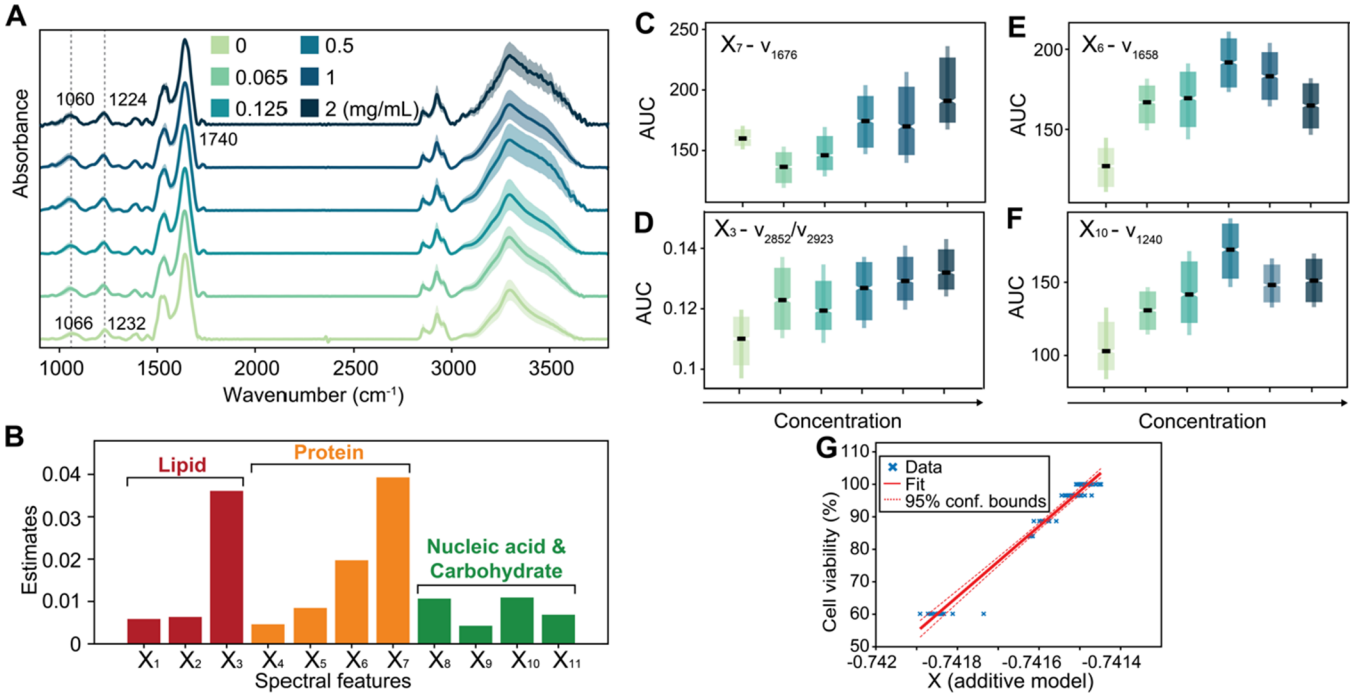

Figure 3. AUC of spectral features as a function of nisin concentration. (A) Average normalized IR spectra, spanning the range of 900−3800 cm^{-1} of A498 cells subjected to an increasing concentration of nisin. The shaded area indicates the standard deviation. The corresponding color-coded variations are indicated in the legend. (B) Assessment of AUC between different nisin-treated groups to inform the spectral features. (C−H) AUC of the top six spectral features is based on the estimates. Violin plots depict the distribution of individual data sets. The middle line inside the box indicates the median, the upper and lower edges of the box indicate the first and third quartiles, and the whiskers extend to 1.5× the interquartile. (G) Fitted multivariate regression model. Additive regression model with the corresponding fit and 95% confidence bounds (partial regression leverage plot).

nucleic acids and leads to the opaqueness of samples for accurate IR detection.[43]

Previous studies have reported contradictory findings on the dependence of the DNA and RNA absorbance peak intensity with cell apoptosis.[42,44] While it is debatable whether cell apoptosis causes an increase or decrease of the nucleic acid absorbance in the IR spectra, we divide the AUC at 1080 and 1240 cm^{-1} to normalize the variability and observe an overall elevation in the ratio with the increasing incubation with the *L. lactis* bead (Figure 2C). Our findings align with a previous study that highlighted the sensitivity of band ratio and may be considered a satisfactory biomarker to reveal the progression of cell apoptosis, which is as evidenced by chromatin condensation and the possible reduction of protein disulfide bond.[48] For evaluating the lipid compositions, the spectral features prominently appear within the 2820−3000 cm^{-1} region, partially contributed by the CH groups on proteins and other molecules. In Figure 2D, E, two wavenumbers at 2852 and 2923 cm^{-1} usually represent the symmetric and asymmetric methylene groups on the membrane lipids. However, there is little change in the group treated with the *L. lactis* bead, whereas the groups with empty beads or *E. coli* beads have a more drastic change. A similar trend is also found in Figure 2F with the AUC ratio at 2852 and 2923 cm^{-1}. For analyzing the protein secondary structure, we note an increasing trend in the parallel β-sheet (1622 cm^{-1}) (Figure 2G) while a decreasing trend in random coil (1642 cm^{-1}) and α-helix (1658 cm^{-1}) structures between 24 and 48 h (Figure 2H, I) in the group treated with *L. lactis* beads. Overall, Figure 2 shows the variability of chemical composition changes with an unpredictable pattern. Since the interaction of probiotics and cancer cells is dynamic involving numerous factors, the impacts on several macromolecules are ambiguous. Since the key difference in the culture medium of the *E. coli* beads and *L. Lactis* beads is the presence of nisin, our goal was to understand the impact of nisin on cell apoptosis. To further investigate the distinctive changes of the macromolecules during cell apoptosis, we simplified the system by treating A498 cells with nisin at different concentrations.

Identification of Significant Spectral Features Related to Cell Apoptosis. Nisin is one of the most prominent compounds secreted by probiotics that provoke intrinsic pathways of cell apoptosis.[40,49] To establish a commensurate relationship between the impact of nisin on cell apoptosis, cells were treated with varying concentrations of free nisin between 0 and 2 mg/mL and imaged by an IR microscope and spectra recorded (Figures 3A and S7). On the other hand, the morphological changes on the A498 cells during apoptosis were observed by brightfield imaging, and the cell viability was quantified by WST-1 assay (Figure S8). Eventually, the IR spectral features are to be correlated to the biological values in our analyses. Specifically, we focus on monitoring three spectral regions, namely, 998−1120, 1560−1700, and 2820−3000 cm^{-1}, which are associated with carbohydrates and nucleic acids, proteins, and lipids, respectively. In the 998−1120 cm^{-1} region, two peaks were observed to downshift from 1066 to 1060 cm^{-1}, and from 1232 to 1224 cm^{-1}, respectively. Furthermore, an absorbance peak was noted to emerge around 1740 cm^{-1} after the cells were treated with nisin. This peak usually refers to the base-paired DNA strands[50] and the ester group (C=O) in the lipid.[44] These characteristics are indicative of biochemical and biophysical changes during cell apoptosis.

https://doi.org/10.1021/acs.analchem.4c00894
Anal. Chem. XXXX, XXX, XXX−XXX

To further investigate the detailed molecular conformational changes, we used a curve-fit model for multiple Gaussian bands in these specified regions. Assigned peak positions for fitting are referenced from previous studies as an initial approximation.[50−52] The results after the deconvolution are shown in Figures S9−S11. The best fits of peak positions for each spectral region are listed in Table S1, with the corresponding molecular assignments. To determine the primary spectral features among various biomolecules, we developed a regression tree model to predict the spectral positions (and the corresponding AUC) that have the most significant contribution to explaining changes with respect to the nisin dosages. Figure 3B shows estimates of predictor importance. The changes in the mean squared error (MSE) due to splits on every predictor are summed and then divided by the number of branch nodes for each predictor. Our analysis identified 11 prominent features with a combination of wavenumbers referring to protein secondary structure, lipid, and nucleic acid. These factors are related to the hallmark of cell apoptosis including cytoskeletal breakdown, DNA fragmentation, and membrane blebbing (Table S1). The AUC of the selected spectral features was plotted to visualize the trend where there was either an increase or decrease in the values (Figures 3C−F and S12). Next, based on the predictor importance analysis, the selected spectral features are collectively modeled to represent conformational changes in lipids, proteins, nucleic acids, and carbohydrates as a measure to correlate with the degree of cell viability.

The absorption in the spectral region 1560−1700 cm^{-1} in biological structures, often referred to as the Amide I band, commonly represents the superimposition of protein secondary structures.[51] The amide I band is sensitive to the molecular geometry and hydrogen bonding of protein molecules and provides information about different C=O stretching frequencies for various structural components. In our study, the Amide I band was mainly assumed to have contributions from all types of secondary structures including β-sheet, random coil, α-helix, and β-turn structures. Based on the predictor importance plot, it is apparent that the protein secondary structure, especially β-turns, α-helices, and random coils, have the most prominent contributions with regard to the degree of apoptosis. With the increasing degree of cell apoptosis, there is an increase in β-turns and a complementary trend between α-helices and random coils content (Figures 3C, E and S13). The conformational changes in the protein secondary structures due to protein misfolding and aggregations are influenced by a variety of factors, including morphological changes associated with cell apoptosis, alterations in chromatin induced by DNA damage, DNA−protein interaction, and the expression of a cascade of enzymes related to the signaling pathway.[53]

The spectral range of 2820−3000 cm^{-1} is primarily associated with lipids. Figure 3D shows the increasing trend in the ratio of AUC at 2852 and 2923 cm^{-1}, characteristic of symmetric and antisymmetric stretching modes of methylene groups (CH_2) on the acyl chains, respectively, as a function of increasing concentrations of nisin. These changes can be attributed to alterations in the lipid composition and structure of the plasma membrane, which can lead to an increase in membrane fluidity during apoptosis, resulting in the formation of vesicles, blebs, and apoptotic bodies.[43,54] This process is facilitated by the outward flipping of phosphatidylserine (PS), a key marker of apoptotic cells, on the outer surface of the plasma membrane. Additionally, since apoptosis is usually triggered as an oxidative stress, unsaturated lipids are particularly susceptible to lipid peroxidation. Moreover, the organelles, such as mitochondria and endoplasmic reticulum, are also rich in unsaturated lipids and can be vulnerable to oxidative stress.[50] The spectral region between 998 and 1120 cm^{-1} is mainly associated with macromolecules such as carbohydrates and all forms of nucleic acids (RNA and DNA), where we see a gradual increase in the AUC at 1240 cm^{-1} with elevated nisin concentrations (Figure 3F). The AUC value at 1055 cm^{-1} elevates initially followed by a slight decrease after the concentration passes 0.5 mg/mL. It is important to monitor structural changes of RNA and DNA, as they play pivotal roles in protein synthesis, genetic information storage, and the replication and transfer of genetic material. As the cells undergo shrinkage during apoptosis, various phenomena such as DNA fragmentation and chromatin condensation also occur.

Furthermore, the large fraction of DNA breaks down into smaller sizes from 50 to 300 kbp or even oligonucleosomal fragments based on the findings from DNA ladder characterization.[44] To account for the inherent variability in the data, we employed a nonlinear model for establishing a correlation analysis between the absorbance of the spectral features and cell viability. This approach allows us to capture the complex relationships and variations in the data set more accurately.

Relationship between the Selected Spectral Features and Cell Apoptosis. We sought to establish a relation between the observed important wavenumbers and apoptosis via a multivariate regression model. Our results show that apoptosis is well-described by the regression model (Figure 3G) using experimental data summarized by our selected spectral features. Different x-variables, namely C (y-intercept), X_3 (lipid ratio), X_9 (1080 cm^{-1}), X_{10} (1240 cm^{-1}), *and* X_{11} (nucleic acid ratio) show higher contributions based on the coefficient plot (Figure S15). $\hat{Y}$ is the estimated response (predictor value), and β_p is the fitted coefficients. The coefficients are estimated to minimize the mean squared differences between the prediction vector $\hat{Y}$ and the true response vector Y, that is $\hat{Y}-Y$. Under the assumptions based on noise, these coefficients also maximize the likelihood of the prediction vector. Our results show that nucleic acid changes were significantly associated with cell viability, with a smaller p-value indicating greater evidence against the null hypothesis. On the other hand, variables X_1 (2852 cm^{-1}), X_4 (1622 cm^{-1}), and X_5 (1642 cm^{-1}) have negligible effects on the prediction, with coefficient estimates close to zero. Next, we visualize the relationships between a selected predictor, X_i, and predicted responses, Y, using the individual conditional expectation plots in Figure S14. The features such as at X_1, X_4, and X_5, individually, do not show much contribution to the model and hence the predicted cell viability but collectively influence the model. Additionally, the multivariable logistic regression demonstrates that lipids and DNA secondary structures are significantly associated with higher cell viability. Overall, more parameters related to cell apoptosis or other biological activities may need to be included in the model for better predictions and further refinements. Here, we demonstrate a simple approach to predict cell apoptosis without any labeling merely with eight spectral features and their correlations.

https://doi.org/10.1021/acs.analchem.4c00894
Anal. Chem. XXXX, XXX, XXX−XXX

CONCLUSIONS

Overall, this study highlights new analytical approaches combined with a dynamic cocultivation system to elucidate the interplay between probiotic bacteria (*L. lactis* and *E. coli*) and cancer cells, using A498 kidney cancer cells as a model system. The methodology of probiotics encapsulation provides a favorable 3D environmental niche with biofilm-like confinement while maintaining structural integrity without bacteria leakage during the culture. In particular, the use of IR spectral features provides technological insight into cellular dynamics to monitor changes in structural groups in DNA and protein secondary structures. We demonstrate the diagnostic capability of FT-IR spectroscopy to observe the overall biological variations in a coculture system by monitoring cell apoptosis. Changes in three mid-IR spectral regions can serve as biomarkers for cell apoptosis: (1) an increase in the lipid ratio, (2) an increase in the β-turns structure of the total cellular protein, and (3) an increase in the ratio of nucleic acid ratio. By assessing multiple biomolecular parameters simultaneously with IR spectroscopy, a mathematical correlation between spectroscopic difference and the percentage of cell viability could be established. Despite the inherent variability present in biological systems, we identified a significant correlation between the important spectral features and the degree of cell viability. Our finding highlights the potential of using spectral features as quantitative biomarkers to assess and predict cellular viability in similar biological systems. As IR spectroscopy requires minimal sample handling with high sensitivity, it could be a promising tool to provide a holistic picture of the cell status. The reported studies will inspire approaches for monitoring dynamic and complex microbe-host cell interactions in biological systems via IR spectroscopic imaging.

ASSOCIATED CONTENT

Supporting Information

The Supporting Information is available free of charge at https://pubs.acs.org/doi/10.1021/acs.analchem.4c00894.

Additional experiment methods, analysis of probiotics encapsulated hydrogel beads cocultured with A498 cells, and analysis of FT-IR spectra (PDF)

AUTHOR INFORMATION

Corresponding Authors

Rohit Bhargava − *Department of Bioengineering, Department of Electrical and Computer Engineering, Cancer Center at Illinois, Beckman Institute for Advanced Science and Technology, and Departments of Mechanical Science and Engineering, Chemical and Biomolecular Engineering, and Chemistry, University of Illinois at Urbana−Champaign, Urbana, Illinois 61801, United States;* orcid.org/0000-0001-7360-994X; Email: rxb@illinois.edu

Joseph Irudayaraj − *Department of Bioengineering, Cancer Center at Illinois, and Beckman Institute for Advanced Science and Technology, University of Illinois at Urbana−Champaign, Urbana, Illinois 61801, United States; Carl R. Woese Institute for Genomic Biology, University of Illinois at Urbana−Champaign, Urbana, Illinois 61801, United States; Biomedical Research Center, Mills Breast Cancer Institute, Carle Foundation Hospital, Urbana, Illinois 61801, United States;* orcid.org/0000-0002-0630-1520; Email: jirudaya@illinois.edu

Authors

Yoon Jeong − *Department of Bioengineering and Cancer Center at Illinois, University of Illinois at Urbana−Champaign, Urbana, Illinois 61801, United States; Biomedical Research Center, Mills Breast Cancer Institute, Carle Foundation Hospital, Urbana, Illinois 61801, United States;* orcid.org/0000-0002-9309-8312

Pei-Hsuan Hsieh − *Department of Bioengineering and Beckman Institute for Advanced Science and Technology, University of Illinois at Urbana−Champaign, Urbana, Illinois 61801, United States*

Yamuna Phal − *Departments of Electrical Engineering and Quantitative Biosciences and Engineering, Colorado School of Mines, Golden, Colorado 80401, United States; Colorado Clinical & Translational Sciences Institute, Aurora, Colorado 80045, United States*

Complete contact information is available at: https://pubs.acs.org/10.1021/acs.analchem.4c00894

Author Contributions

[¶]Y.J. and P.-H.H.: contributed equally.

Notes

The authors declare no competing financial interest.

ACKNOWLEDGMENTS

Research reported in this publication was supported by the National Institute of Biomedical Imaging and Bioengineering of the National Institutes of Health (NIH) under Award Numbers T32EB019944.

REFERENCES

(1) Fong, W.; Li, Q.; Yu, J. *Oncogene* **2020**, *39*, 4925−4943.
(2) Sepich-Poore, G. D.; Zitvogel, L.; Straussman, R.; Hasty, J.; Wargo, J. A.; Knight, R. *Science* **2021**, *371* (6536), No. eabc4552.
(3) Karin, M.; Jobin, C.; Balkwill, F. *Nat. Med.* **2014**, *20*, 126−127.
(4) Elkrief, A.; Derosa, L.; Kroemer, G.; Zitvogel, L.; Routy, B. *Ann. Oncol.* **2019**, *30*, 1572−1579.
(5) Cheng, W. Y.; Wu, C. Y.; Yu, J. *Gut* **2020**, *69*, 1867−1876.
(6) Mountcastle, S. E.; Cox, S. C.; Sammons, R. L.; Jabbari, S.; Shelton, R. M.; Kuehne, S. A. *J. Oral Microbiol.* **2020**, *12*, No. 1773122.
(7) Din, M. O.; Danino, T.; Prindle, A.; Skalak, M.; Selimkhanov, J.; Allen, K.; Julio, E.; Atolia, E.; Tsimring, L. S.; Bhatia, S. N.; Hasty, J. *Nature* **2016**, *536*, 81−85.
(8) Hong, J. W.; Song, S.; Shin, J. H. *Lab Chip* **2013**, *13*, 3033−3040.
(9) Phal, Y.; Pfister, L.; Carney, P. S.; Bhargava, R. *J. Phys. Chem. C* **2022**, *126*, 9777−9783.
(10) Phal, Y.; Yeh, K.; Bhargava, R. *Appl. Spectrosc.* **2021**, *75*, 1067−1092.
(11) Lux, L.; Phal, Y.; Hsieh, P. H.; Bhargava, R. *Appl. Spectrosc.* **2022**, *76*, 105−117.
(12) Hsieh, P.-H.; Phal, Y.; Prasanth, K. V.; Bhargava, R. *Anal. Chem.* **2023**, *95*, 3349−3357.
(13) Morrish, R. B.; Hermes, M.; Metz, J.; Stone, N.; Pagliara, S.; Chahwan, R.; Palombo, F. *Front. Cell Dev. Biol.* **2019**, *7*, 141.
(14) Chan, K. L. A.; Fale, P. L. V. *Anal. Chem.* **2014**, *86*, 11673−11679.
(15) Shi, L.; Liu, X.; Shi, L.; Stinson, H. T.; Rowlette, J.; Kahl, L. J.; Evans, C. R.; Zheng, C.; Dietrich, L. E. P.; Min, W. *Nat. Methods* **2020**, *17*, 844−851.
(16) Bhargava, R. *Annu. Rev. Anal. Chem.* **2023**, *16*, 205−230.
(17) Wrobel, T. P.; Bhargava, R. *Anal. Chem.* **2018**, *90*, 1444−1463.
(18) Damayanti, N. P.; Craig, A. P.; Irudayaraj, J. *Analyst* **2013**, *138*, 7127−7134.

(19) Yu, C.; Gestl, E.; Eckert, K.; Allara, D.; Irudayaraj, J. *Cancer Detect Prev.* **2006**, *30*, 515−522.
(20) Oust, A.; Møretrø, T.; Kirschner, C.; Narvhus, J. A.; Kohler, A. *J. Microbiol. Methods* **2004**, *59*, 149−162.
(21) Wenning, M.; Scherer, S. *Appl. Microbiol. Biotechnol.* **2013**, *97*, 7111−7120.
(22) Alruwaili, M. A. *Am. J. Agric. Biol. Sci.* **2013**, *8*, 135−141.
(23) Gupta, M.; Irudayaraj, J.; Schmilovitch, Z.; Mizrach, A. *Trans. ASABE* **2006**, *49*, 1249−1255.
(24) Yang, H.; Irudayaraj, J. *J. Mol. Struct.* **2003**, *646*, 35−43.
(25) Yu, C.; Irudayaraj, J. *Trans. ASABE* **2006**, *49*, 1623−1632.
(26) Yu, C.; Irudayaraj, J. *Biopolymers* **2005**, *77*, 368−377.
(27) Sivakesava, S.; Irudayaraj, J.; Demirci, A. *J. Ind. Microbiol. Biotechnol.* **2001**, *26* (4), 185−190.
(28) Sivakesava, S.; Irudayaraj, J.; Ali, D. *Process Biochem.* **2001**, *37*, 371−378.
(29) Sakhamuri, S.; Bober, J.; Irudayaraj, J.; Demirci, A. Simultaneous Determination of Multiple Components in Nisin Fermentation Using FTIR Spectroscopy *Process Biochem.* 2001, *37*.
(30) Paradkar, M. M.; Irudayaraj, J. *Int. J. Dairy Technol.* **2002**, *55*, 127−132.
(31) Davis, R.; Irudayaraj, J.; Reuhs, B. L.; Mauer, L. J. *J. Food Sci.* **2010**, *75* (6), M340−M346.
(32) Jeong, Y.; Kong, W.; Lu, T.; Irudayaraj, J. *Biosens. Bioelectron.* **2023**, *219*, No. 114809.
(33) Jeong, Y.; Irudayaraj, J. *ChemComm.* **2022**, *58*, 8584−8587.
(34) Jeong, Y.; Irudayaraj, J. *Acta Biomater.* **2023**, *158*, 203−215.
(35) Jeong, Y.; Han, X.; Vyas, K.; Irudayaraj, J. *ACS Appl. Mater. Interfaces* **2024**, *16*, 28093−28103, DOI: 10.1021/acsami.4c02568.
(36) Ahmadi, S.; Ghollasi, M.; Hosseini, H. M. *Microb. Pathog.* **2017**, *111*, 193−197.
(37) Goldstein, A.; Kapelner, A.; Bleich, J.; Pitkin, E. *J. Comput. Graph. Stat.* **2015**, *24*, 44−65.
(38) Holland, P. W.; Welsch, R. E. *Commun. Stat. Theory Methods* **1977**, *6*, 813−827.
(39) Harris, L. J.; Fleming, H. P.; Klaenhammer, T. R. *Appl. Environ. Microbiol.* **1992**, *58*, 1477−1483.
(40) Joo, N. E.; Ritchie, K.; Kamarajan, P.; Miao, D.; Kapila, Y. L. *Cancer Med.* **2012**, *1*, 295−305.
(41) Arakawa, H.; Neault, J. F.; Tajmir-Riahi, H. A. *Biophys. J.* **2001**, *81*, 1580−1587.
(42) Gasparri, F.; Muzio, M. *Biochem. J.* **2003**, *369*, 239−248.
(43) Zelig, U.; Kapelushnik, J.; Moreh, R.; Mordechai, S.; Nathan, I. *Biophys. J.* **2009**, *97*, 2107−2114.
(44) Liu, K.-Z.; Jia, L.; Kelsey, S. M.; Newland, A. C.; Mantsch, H. H. *Apoptosis* **2001**, *6*, 269−278.
(45) Guo, M.; Lu, B.; Gan, J.; Wang, S.; Jiang, X.; Li, H. *Cell Cycle* **2021**, *20*, 1033−1040.
(46) Banfalvi, G. *Apoptosis* **2017**, *22*, 306−323.
(47) Martinez, M. M.; Reif, R. D.; Pappas, D. *Anal. Methods* **2010**, *2*, 996−1004.
(48) Oldenhof, H.; Schütze, S.; Wolkers, W. F.; Sieme, H. *Andrology* **2016**, *4*, 430−441.
(49) Shin, J. M.; Gwak, J. W.; Kamarajan, P.; Fenno, J. C.; Rickard, A. H.; Kapila, Y. L. *J. Appl. Microbiol.* **2016**, *120*, 1449−1465.
(50) Liu, K.-Z.; Mantsch, H. H. *J. Mol. Struct.* **2001**, *565*, 299−304.
(51) Kong, J.; Yu, S. *Acta Biochim. Biophys. Sin. (Shanghai)* **2007**, *39*, 549−559.
(52) Krimm, S.; Bandekar, J. *Adv. Protein. Chem.* **1986**, *38*, 181−364.
(53) Li, J.; Yuan, J. *Oncogene* **2008**, *27*, 6194.
(54) Mihoubi, W.; Sahli, E.; Gargouri, A.; Amiel, C. *PLoS One* **2017**, *12*, No. e0180680.

https://doi.org/10.1021/acs.analchem.4c00894
Anal. Chem. XXXX, XXX, XXX−XXX